Chapter 4

4.1 Introduction

The multiferroic properties of $BiFeO_3$ could be successfully altered with the substitution of rare earth ions at Bi-site. Bi-site substitution alters the bonding strength of Fe-O bond due to the competency between Fe-O and Bi-O bond. The aliovalent alters the band width which in turn modifies the tolerance factor. In this study Gd is optimized for substitution on the Bi-site of $Bi_{0.9}Sm_{0.1}FeO_3$ system in order to enhance the magnetic and dielectric properties simultaneously.

As Gd^{3+} has lager effective magnetic moment (7.9 μB) that cause considerable lattice distortion with smaller ionic radius than that of Bi^{3+} (Gd^{3+}: 0.938 Å, CN 8; Bi^{3+}: 1.17 Å, CN 8) [Tang *et al.* 2016; Khomchenko *et al.* 2009].

The polycrystalline samples of $Bi_{0.9-x}Sm_{0.1}Gd_xFeO_3$ (x =0.0, 0.025, 0.050, 0.075, 0.1) were prepared using a solid-state ceramic route. The microstructural, dielectric and magnetic properties have been investigated. The magnetic parameters are measured at maximum of 60 kOe applied magnetic field. Dielectric studies at room temperature are discussed in the range of 20Hz -1MHz while high temperature studies carried out up to 600K at frequency range between 20Hz to 1MHz.

In order to check the instability of the structure of Gd substituted BSFO perovskite the tolerance factor is calculated using equation 1.1 as shown in fig. 4.1. Theoretically, it predicts the alteration of one electron band width in the proposed compositions.

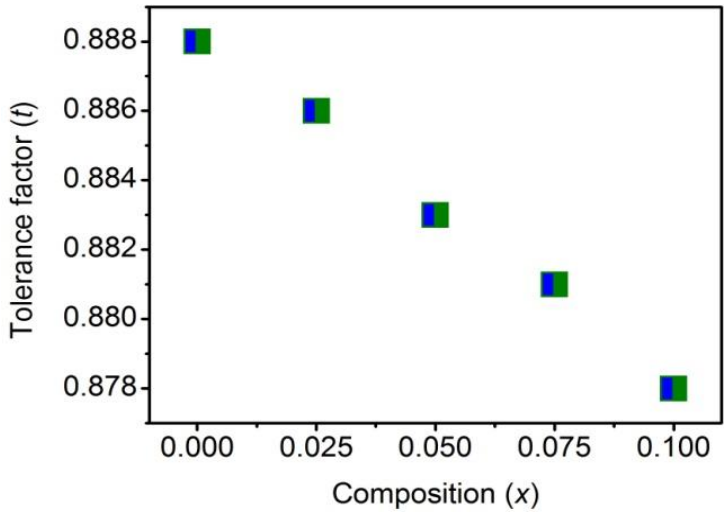

Fig. 4.1: Tolerance factor of $Bi_{0.9-x}Gd_xSm_{0.1}FeO_3$ (x =0.0, 0.025, 0.050, 0.075, 0.1).

4.2 Results and discussion

4.2.1 X-ray diffraction

Fig. 4.2 (a and b) shows the room temperature X-ray patterns of the Gd substituted BSFO samples. Also, shows the indexing of the peaks at diffraction angles $2\theta \approx 22°$, 32°, 39°, 45°, 57° after matching with the standard JCPDS file (#14-0181) *i.e.*, belonging to rhombohedral (R3c) space group [Woodward *et al.*1997]. The secondary phase of $Bi_{2.46}Fe_5O_{12}$ is observed for the samples $x \geq 0.075$ [Sharma *et al.* 2016]. It is also noticed in Fig. 2 (b) that for $x \geq 0.075$, the merging of split peaks (110/104) started that indicates the formation of pseudocubic phase along with the evolution of other impurity phases. Fig. 4.3 (a) shows the lattice parameters '*a*' and '*c*' were calculated from X-ray diffractograms. It is observed that both the lattice parameters '*a*' and '*c*' are decreased with the increasing Gd content. For the value of x = 0.025 a sudden increment in '*a*' and decrement in '*c*' shows the symmetry changes signifying the presence of pure rhombohedral phase up to 14% of double substitution in the pure $BiFeO_3$ system.

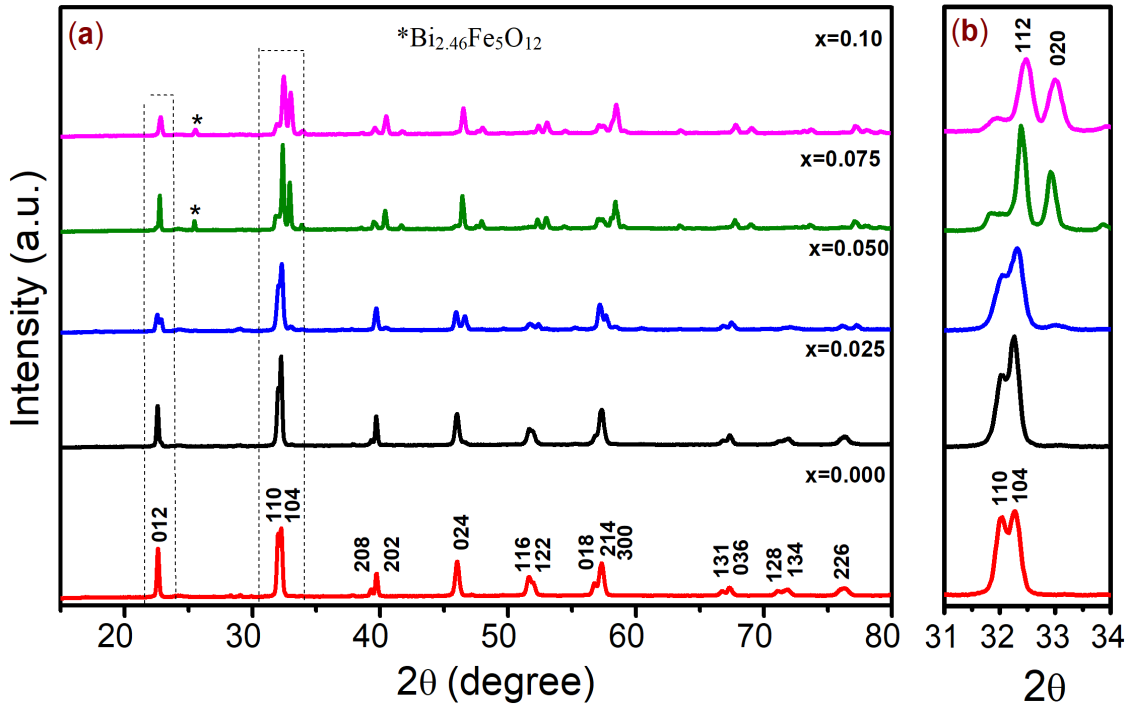

Fig. 4.2: (a) XRD graphs of $Bi_{0.9-x}Gd_xSm_{0.1}$ Fe O_3 (x = 0.0 - 0.1), and (b) magnified pattern of peaks (104) and (110) at 2θ = 32°- 34°.

Fig. 4.3 (a-c) region (I) shows the solubility limit and region (II) is after the solubility limit. After the solubility limit, the decrease in '*a*' and '*c*' is observed due to secondary phases. To support the estimation of the solubility limit, the intensity is shown as a function of composition in Fig. 4.3(b). It is noticed that the intensity of peaks (110) decreases and (104) increases in the region (I) up to x = 0.05. In region (II), for x ≥ 0.075, the peak (110) starts splitting due to the evolution of secondary phases. The effect of substitution on the structure is also estimated with strain and crystallite size calculation. The strains due to defects were calculated using the Williamson-Hall model according to the following Eq. 4.1:

$$\beta cos\theta = \frac{0.89\,\lambda}{D} + 4\varepsilon sin\theta \qquad (4.1)$$

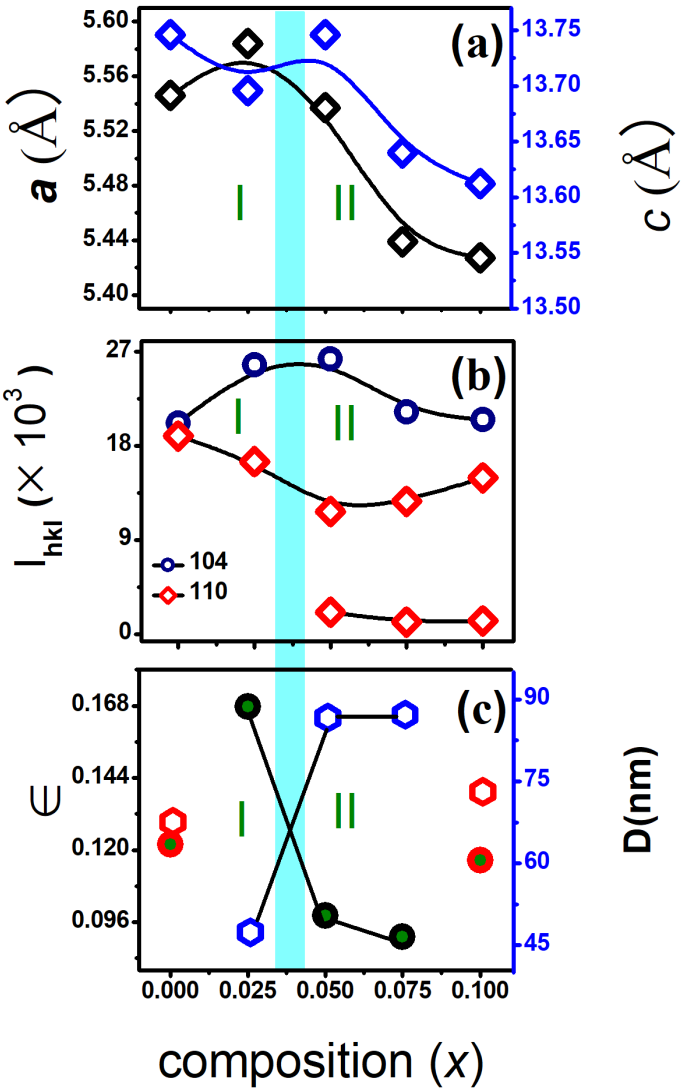

Fig. 4.3: (a) Variation of lattice parameters with x, (b) Variation of Intensity I_{hkl} for peaks (104) & (110) with x, and (c) Variation of microstrain and Crystallite size for $Bi_{0.9-x}Sm_{0.1}Gd_xFeO_3$ (x =0.0 - 0.1).

Fig. 4.3 (c) shows the variation of microstrain and crystallite size with x. The average crystallite size (*D*) and microstrain (∈) were calculated by using above expression where *β* is the full-width half-maximum at the Bragg angle (*2θ*) and wavelength (*λ*) of Cu Kα X-ray radiation. Microstrain and crystallite size were obtained from the slope and the intercept of β

cosθ vs 4sinθ (graph not shown here). It is found that the microstrain decreases suggesting the local distortion due to BiO_6 octahedra leading to the structural changes. Thus, for $x \geq 0.075$ the secondary phases dominated which led to a reduction in the tetragonality. This is also indicating the solubility of the sample is lying between x=0.025 and x=0.05 which is in correlation with the standard literature [Jha *et al.* 2014].

4.2.2 Density measurement

Fig. 4.5 shows the relative density of pure BFO and Gd substituted BSFO samples where bulk density is measured using the Archimedes principle. It is revealed that the density increased up to the MPB limit of the pure BFO samples and observed that the substituted samples are more than 95% dense. Further, increase in Gd content results in decrement of relative density due to the formation of secondary phases ($Bi_{2.46}Fe_5O_{12}$) and ($Bi_2Fe_4O_9$).

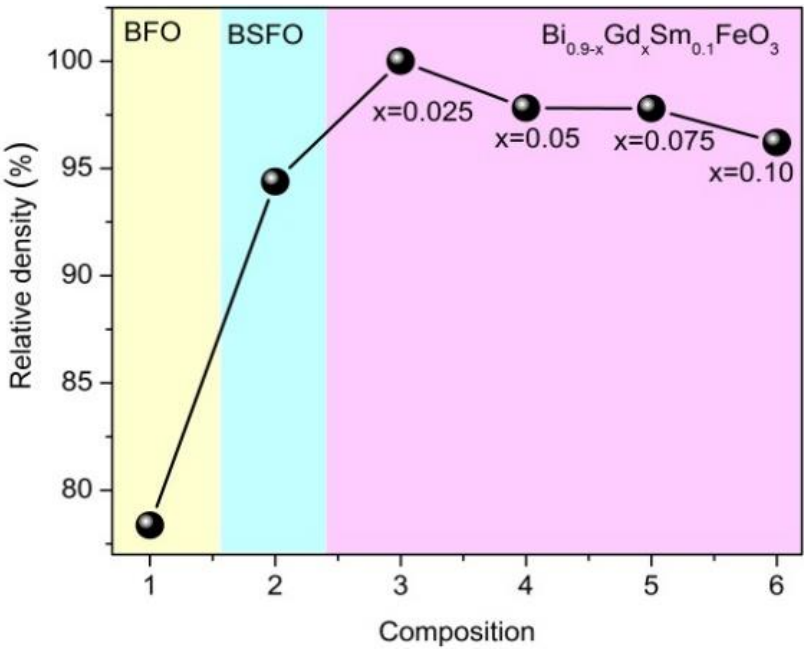

Fig. 4.4: Relative density of pure BFO and Gd substituted BSFO samples.

4.2.3 Morphological studies

The morphology of the studied samples $Bi_{0.9-x}Sm_{0.1}Gd_xFeO_3$ (x =0.0, 0.025, 0.050, 0.075, 0.1) were studied on the basis of scanning electron microscopic images (20 KX magnification) shown in Fig. 4.5(a - e). The grains are of various sizes and irregular in shape. Moreover, some grains grow abnormally and agglomerated after high-temperature heat treatment or either accumulation of dopant ions in the grain boundaries [Xue *et al.* 2014; Ablat *et al.* 2014]. It is clearly observed that with Gd substitution affects the grain sizes drastically. With increasing the Gd concentration the grains become more spherical so density all the Gd substituted samples are higher than that of pure BFO and BSFO. It is also revealed that the grain sizes increase with Gd substitution up to $x \geq 0.05$ as shown in Fig. 4.6 and thereafter decreases. The decrease in grain sizes can be attributed to the promotion of the nucleation rate tending to suppress the grain growth with substitution [Dong *et al.* 2014].

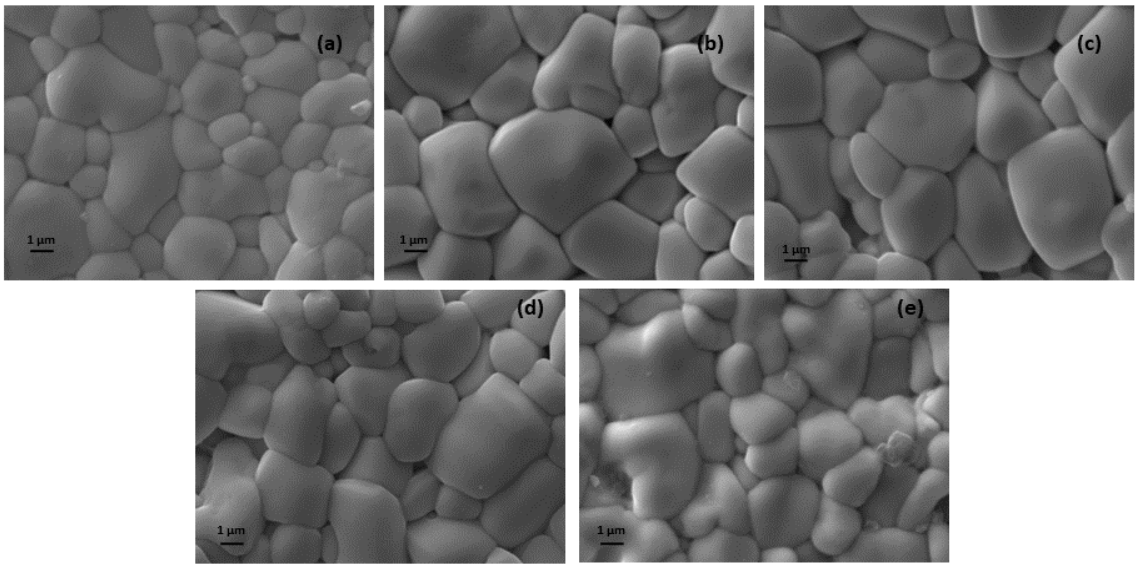

Fig. 4.5 (a-e): SEM images using secondary electrons of $Bi_{0.9-x}Gd_x\,Sm_{0.1}FeO_3$ (x =0.0-0.1).

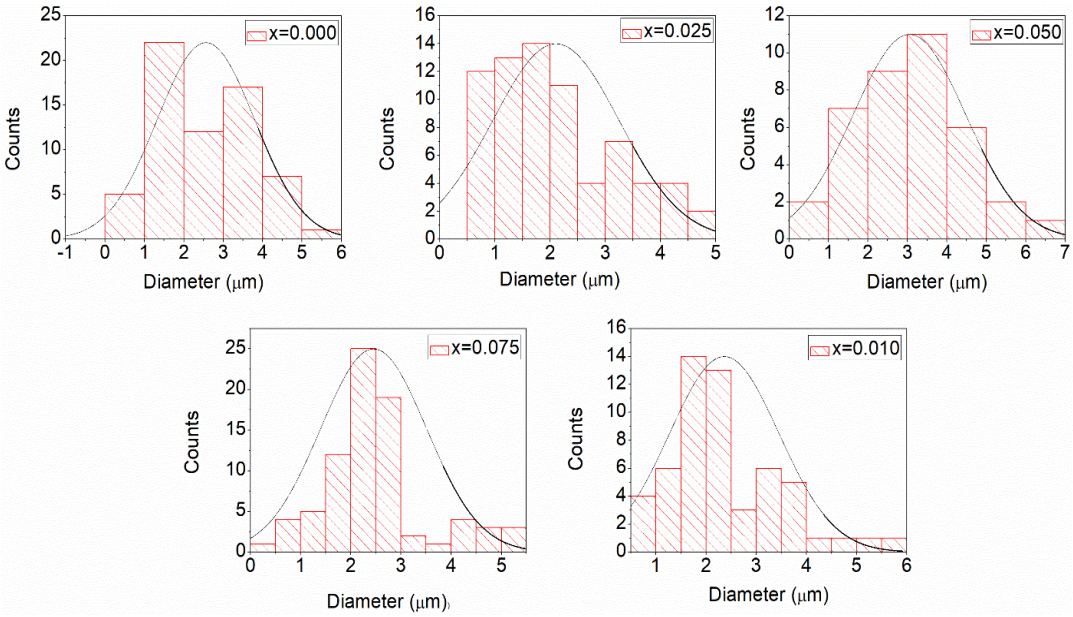

Fig. 4.6: Grain size distribution curves of $Bi_{0.9-x}Gd_x Sm_{0.1}FeO_3$ (x =0.0-0.1)

4.2.4 Optical studies

4.2.4.1 FTIR spectra

Fig. 4.7 shows the FTIR spectra of the studied samples recorded at room temperature in the range of 400-1000 cm^{-1}. It is observed that there are four vibration bands obtained for perovskite system at 817 cm^{-1}, 680 cm^{-1}, 540 cm^{-1}, and 441 cm^{-1}. The strongest absorptive peak is observed in the range of ~540 cm^{-1} corresponds to Fe-O bond stretching for x =0.00-0.025 [Arya *et al.* 2013]. For x ≥ 0.050, the vibration bands shift towards lower wave number and become quite soft due to the diffusion of Fe-O bond stretching with higher concentration of Gd that leads to the formation of the pseudocubic phase which are confirmed by X-ray analysis also [Singh *et al.* 2014, Sharma *et al.* 2016]. The peaks obtained for the absorption band at ~441 cm^{-1} corresponds to O-Fe-O bending and at 683 cm^{-1}, 817 cm^{-1} correspond to

bending vibration mode of Bi_2O_3 [Arya *et al.* 2013]. Also, the force constant and bond length of the studied samples are illustrated in Table 4.1.

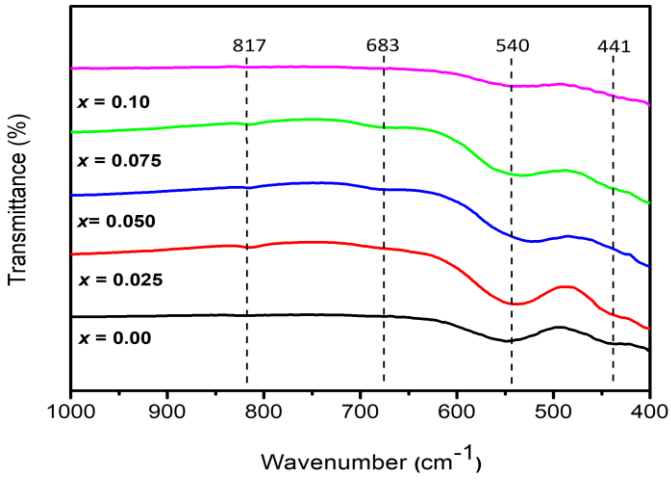

Fig. 4.7: Wavenumber vs. Transmittance of $Bi_{0.9-x}Gd_xSm_{0.1}FeO_3$ (x = 0.0-0.1) samples.

Table 4.1 Force constant (*k*) and bond length of peaks in the range ≈ 538.21 - 549.27 cm^{-1} of $(Bi_{0.9-x}Gd_xSm_{0.1})FeO_3$ (x = 0.0 - 0.1) ceramics.

Composition	Wave no. (cm^{-1})	Effective mass (10^{-26} Kg)	Force constant *k* (N/cm)	Bond length (Fe-O) (Å)
x = 0.00	549.27	2.065	2.2113	1.9737
x = 0.025	540.79	2.065	2.1394	1.9956
x = 0.050	522.36	2.065	1.9996	2.0411
x = 0.075	537.11	2.065	2.1145	2.0033
x = 0.10	533.42	2.065	2.0822	2.0136

The vibration frequency of the Fe-O bond can be determined by using the equations:

$$\nu = \frac{1}{2\pi c}\left(\frac{k}{\mu}\right)^{1/2} \qquad (4.2)$$

Where ν is the wave number, *c* is the velocity of light (3×10^8 m/s), *k* is the average force constant of Fe-O bond and μ is effective mass which can be given as [Singh *et al.* 2014]:

$$\mu = \frac{M_O \times M_{Fe}}{M_O + M_{Fe}} \quad (4.3)$$

Where, M_O and M_{Fe} are atomic weight O and Fe, respectively. The force constant can be calculated by using equation 4.4:

$$k = \frac{17}{r^3} \quad (4.4)$$

Where, r is bond length of Fe-O bond.

4.2.4.2 Ultra-violet visible absorption

Fig. 4.8 shows the variation of absorbance with the wavelength for all the studied samples. The highest absorption peak in the range of ~237nm is due to UV absorption. Other ones are observed in the visible region *i.e.*, ~360-387 nm and ~490-510 nm peaks are assigned to direct band gap peaks *i.e.*, Bi(4d)-O(2p) bonding. The peak at ~672-707 nm corresponds to the d-d transition of Fe (3d) and the peak at ~883-942 nm is due to crystal field transitions [Gowrishankar *et al.* 2016].

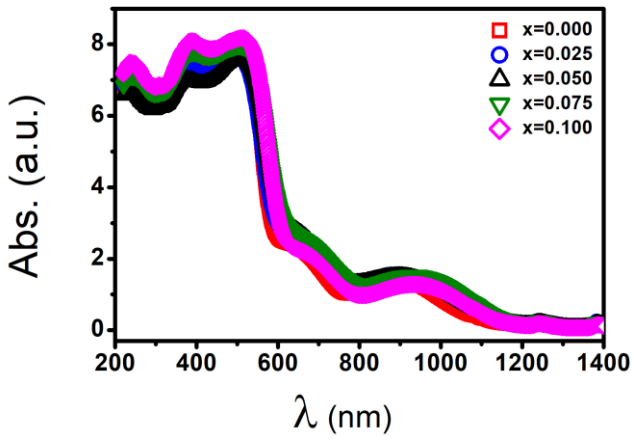

Fig. 4.8: Absorbance spectra of $Bi_{0.9-x}Gd_xSm_{0.1}FeO_3$ (x = 0.0, 0.025, 0.050, 0.075, 0.1).

The direct optical band gap of the Gd substituted samples were calculated using Tauc's relation (Eq. 4.5) and Kubelka–Munk function ($\alpha h\nu^2$) plotted with Energy gap as shown in Fig. 4.8.

$$\alpha h\nu = A\left(h\nu - \mathrm{E_g}\right)^{1/2} \qquad (4.5)$$

Where, α= absorption coefficient, ν= Frequency, h= Planck's constant, E_g= band gap A= absorbance coefficient, n= ½ for direct band gap.

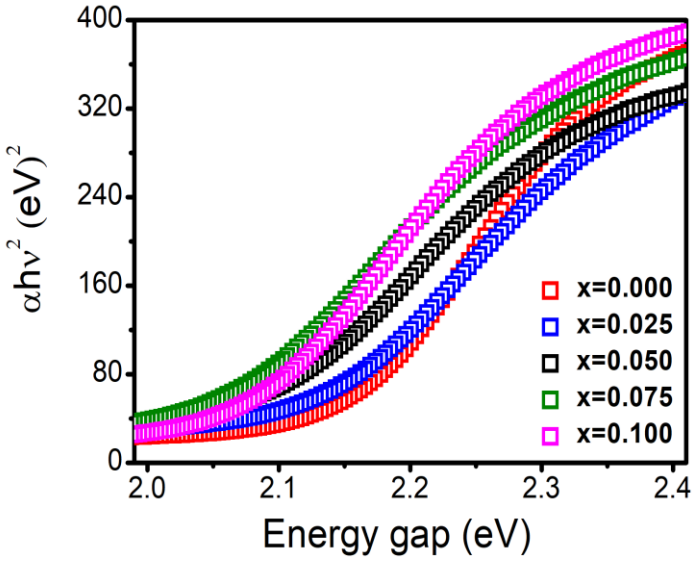

Fig. 4.9: Tauc's plot of $Bi_{0.9-x}Gd_xSm_{0.1}FeO_3$ (x =0.0, 0.025, 0.050, 0.075, 0.1).

Fig. 4.10 shows the variation of band gap with the Gd concentration in the BSFO system. The band gap of pure BFO is ~2.8 eV [Kumar *et al.* 2008]. It is noticed that for pure BSFO the band gap was ~2.1 and with Gd substitution the values were decreases up to x≤0.075. The decrement in the band gap with Gd substitution is due to the size effect. The increment in band gap after x=0.075 confirming the solubility limit and evolution of secondary phases.

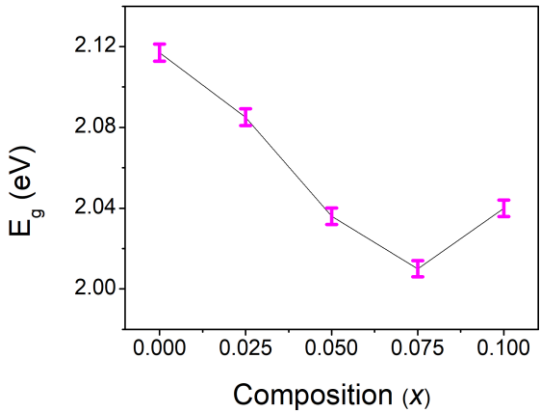

Fig. 4.10: Band gap variation with composition (x =0.0, 0.025, 0.050, 0.075, 0.1).

This solubility limit can be ascribed to the Fe-O stretching observed in FTIR and X-ray diffractograms. Also, this narrow band gap in the visible region for Gd substitution suggests that these compounds are a potential candidate to be used as photocatalysts [Singh *et al.* 2014].

4.2.5 Dielectric studies

4.2.5.1 Room temperature

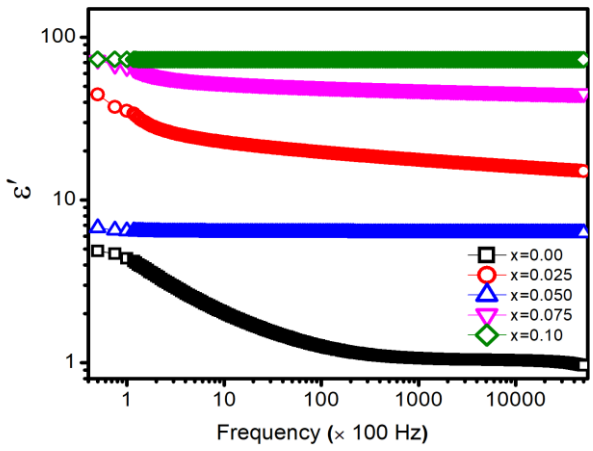

Fig. 4.11: Dielectric constant variation with the Frequency at room temperature of samples $Bi_{0.9-x}Gd_xSm_{0.1}FeO_3$ (x =0.0, 0.025, 0.050, 0.075, 0.1).

The dielectric constant of the Gd substituted BSFO samples are shown in Fig. 4.11. The Dielectric constant (ε') was calculated by using the equation:

$$\varepsilon' = \frac{C \times d}{\varepsilon_{\circ} \times a} \qquad (4.6)$$

Where, ε_o= constant is equal to 8.854×10^{-12}, C= capacitance, a= area, d= distance between two parallel plates.

It is observed that the Gd substituted BSFO systems exhibiting the regular ferroelectric ceramic behavior. The dielectric behavior with frequency can be understood on the basis of Maxwell-Wagner model which suggests at lower frequency space charge polarization is active enough to follow the applied field, a further increase in frequency may not allow them to relax thus, ε' become independent of frequency [Arora *et al.* 2014]. It is observed that dielectric constant increases with the increasing Gd concentrations. At x= 0.05, ε' decreases with due to the formation of an interfacial layer of space charge polarization between two phases as the nucleation of the pseudocubic phase started. This is also coinciding with the solubility limit. Further, increasing Gd content for the value of $x \geq 0.075$, ε' reaches its maximum may be due to the formation of visible impurity phases mainly consisting of garnet type structure attributed to the variation in Fe-O bond length. Hence, the distortion of FeO_6 octahedra may lead to an increase in polarizability in the form of dielectric constant [Godara *et al.* 2015, Vashisth *et al.* 2018].

Fig. 4.12 shows the tangential loss behavior with varying frequency. Generally, the tangential loss of dielectric materials depends on three different factors: space charge polarization, direct current (DC) conduction, and molecular dipole movement [Rayssi *et al.* 2018].

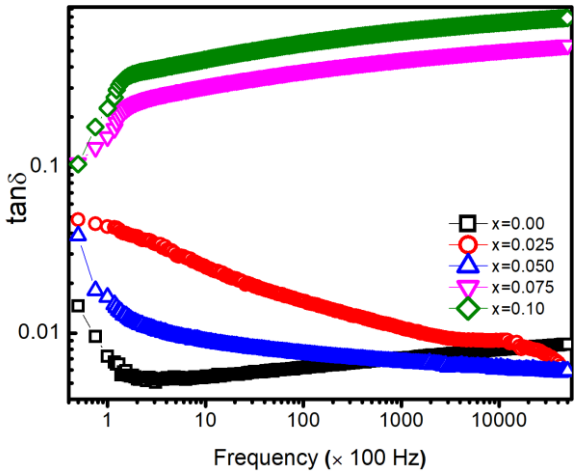

Fig. 4.12: Dielectric loss variation with Frequency at RT of samples $Bi_{0.9-x}Gd_xSm_{0.1}FeO_3$ (x =0.0, 0.025, 0.050, 0.075, 0.1)

It is noticed that the tangential losses are less at low substitution due to less oxygen vacancies and low impurities. The dissipation factor is also following the same trend as ε' as shown in Table 4.2.

Table 4.2 Room temperature dielectric constant (ε') and dissipation factor (tanδ) reported at frequency of 10.5 kHz for $(Bi_{0.9-x}Gd_xSm_{0.1})FeO_3$ (x = 0.0 - 0.1) ceramics.

Parameters	**x = 0.00**	**x = 0.025**	**x = 0.50**	**x = 0.075**	**x = 0.10**
ε'	125	1965	631	4638	6115
tanδ	0.00618	0.0155	0.0074	0.382	0.557

4.2.5.2 High temperature

Fig. 4.13 (a & b) shows the variation of the real part of dielectric permittivity and tanδ with a temperature of pure BFO and Gd (0.0≤ x≤0.1) substituted BSFO samples recorded in the temperature range of 300K to 600K at 50 kHz frequency. It can be seen that

the value of the real part of permittivity and loss is higher for x =0.075 at 300K. It is observed in pure BFO that the value of the real part of dielectric permittivity and tanδ increases up to 450 K leading to the formation of a hump (named as Polomska transition in literature [Jha *et al.* 2015] and thereafter permittivity decreases and loss increases. Further, this kink fades in the real part of dielectric permittivity and loss curves with the Sm substitution and further Gd substitution. Besides, the value of the loss is lower for x =0.05 and x =0.1 showing the reduced leakage current with Gd and Sm substitution.

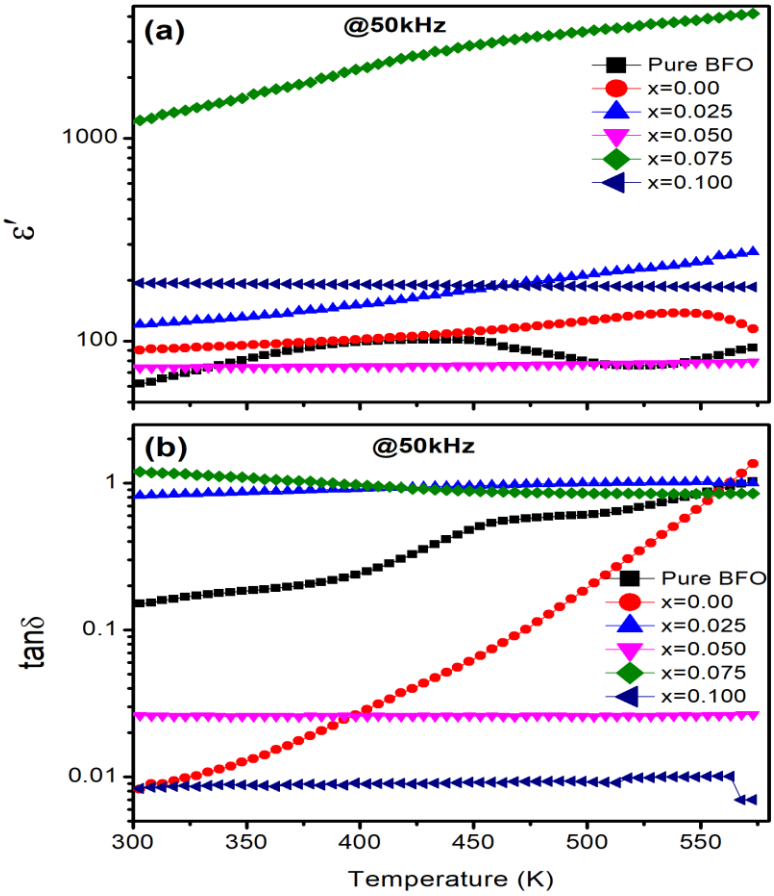

Fig. 4.13: (a) Dielectric constant variation with temperature at 50 kHz Frequency; (b) Dielectric constant variation with temperature at 50 kHz Frequency for samples pure BFO and $Bi_{0.9-x}Gd_xSm_{0.1}FeO_3$ (x =0.0, 0.025, 0.050, 0.075, 0.1).

4.2.5.3 Activation Energy

To verify the conduction mechanism and the correlation of activation energy with the ferroelectric and ferromagnetic properties, Arrhenius plots ($\sigma = \sigma_0 \exp[E_a/KT]$) using ac conductivity extracted from high temperature dielectric curves. The conductivity data is in accordance with the high temperature tanδ curves. Fig. 4.14 depicts the Arrhenius plots for the pure BFO and the substituted samples at frequency of 20 Hz. In pure BFO, the conductivity observed is ~10^{-11} S/cm suggesting that conductivity is not purely ionic in nature, but possesses contributions from electronic/polaronic as well.

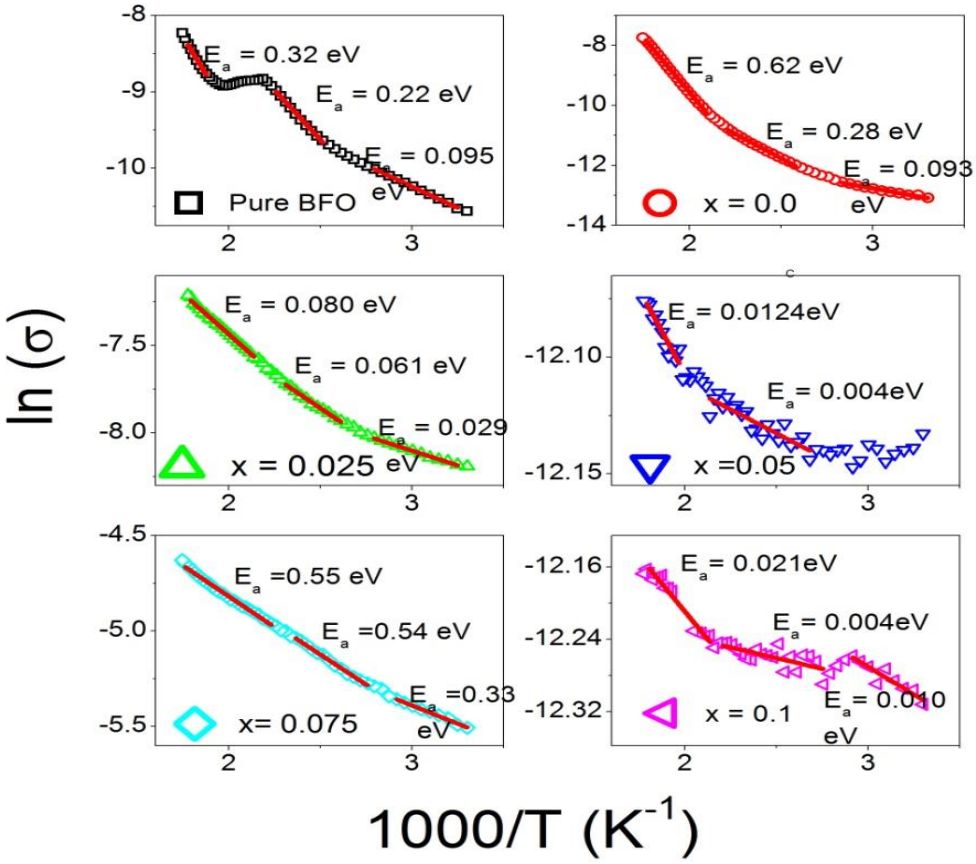

Fig. 4.14: Arrhenius conductivity plots for samples pure BFO and $Bi_{0.9-x}Gd_xSm_{0.1}$ Fe O_3 (x = 0.0, 0.025, 0.050, 0.075, 0.1)

Further, we have observed that in pure BFO, the data is fitted in three regimes with a hump at ~ 450K (Polomska transition [Jha *et al.* 2015]. In the dielectric plots, we observed broad a peak at all frequencies both in the ε' and tan δ curves and the same has been reflected in conductivity plots. Around this transition, E_a changes from 0.32 eV to 0.22 eV showing the formation singly ionized oxygen vacancies [Kumar *et al.* 2020; Dwivedi *et al.* 2001] and the electronic nature of the sample. Further, at high temperature, the activation energy is 95 meV hinting the polaronic conduction.

In Sm =0.1 composition, this Polomska transition fades but the change in activation energy prevails from 0.62 eV to 0.28 eV hinting the conversion from doubly ionized oxygen vacancies to singly ionized oxygen vacancies. Further, at high temperature, polaronic conduction is there. But with the Sm and Gd co-substitution, Polomska transition fades along with the polaronic conduction for all the samples except x =0.075. At x =0.075, highest activation energy is observed in three regimes showing the formation of singly ionized oxygen vacancies. Further, at x =0.075, band gap observed is minimum and magnetization observed is higher, is another important aspect for suppressed dielectric anomalies of bismuth ferrite. This feature accounts for the formation of localized states for oxygen vacancies in between the conduction band and valence band leading to the increase in magnetization. Also, this increase in magnetization is coupled with formation of garnet phase *i.e.,* Fe^{3+} oxidation state.

4.2.6 Ferromagnetic studies

Fig. 4.15 (a) shows the in-plane magnetic behaviour of all the Gd substituted BSFO samples obtained at room temperature. The hysteresis loop shown at applied magnetic field

6T signifies that all the Gd substituted BSFO samples could not achieve saturation magnetization because of uncompensated antiferromagnetic nature [Vashisth *et al.* 2018].

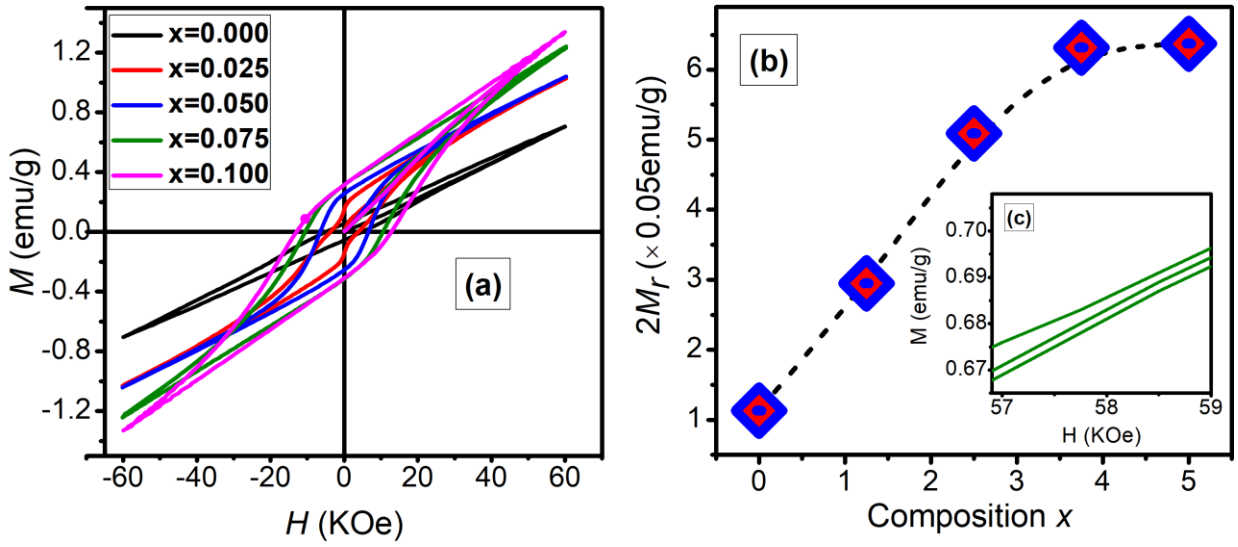

Fig. 4.15 (a): M-H curves of BSFO samples; **(b)** Remanent magnetization variation with the substitution $Bi_{0.9-x}Sm_{0.1}Gd_xFe\ O_3$ (x= 0.0, 0.025, 0.050, 0.075, 0.1); and **(c)** Magnified image of x =0.0, an anti-ferromagnetic nature of hysteresis loop.

The remanent magnetization estimated from the loops and is shown in Fig. 4.15 (b). It is observed that the Remanent magnetization (M_r) increases continuously even after the solubility limit. This can be understood as follows. Firstly, the observed secondary garnet phase ($Bi_{2.46}Fe_5O_{12}$) is famous for higher magnetization *i.e.*, its intensity increases for x ≥ 0.075 leading to the increase in magnetization [Sharma *et al.* 2016]. Secondly, Gd has higher Bohr's Magneton (7.9 μB) so, increasing Gd substitution may form an individual phase which increases remanent magnetization. So, it is expected that Gd substitution could enhance the magnetic properties and suppress the spin cycloid structure of the BSFO system [Basith *et al.* 2017].

4.2.7 Ferroelectric studies

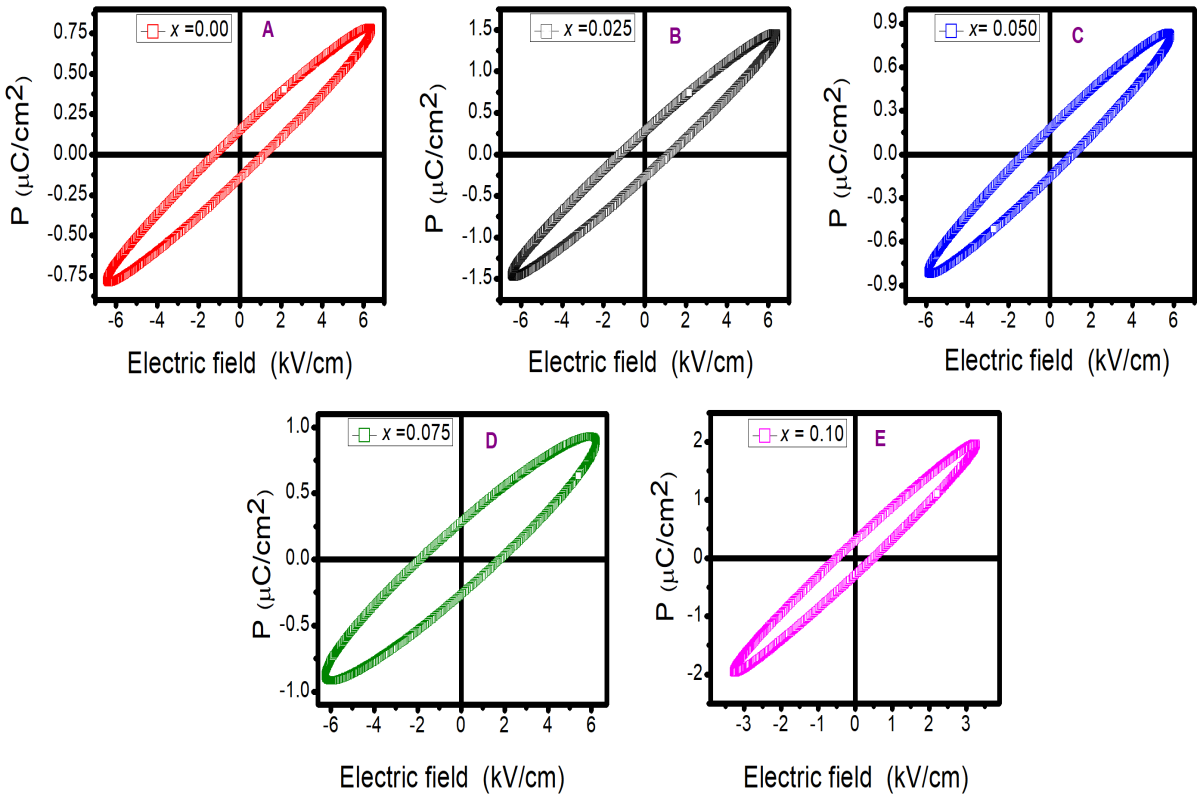

Fig. 4.16 (a-e): P-E loops of $Bi_{0.9-x}Sm_{0.1}Gd_xFe\ O_3$(x= 0.0, 0.025, 0.050, 0.075, 0.1) and **(f):** shows remanent polarization of all the samples.

Fig. 4.16 (a-e) shows the room temperature polarization hysteresis (variation of electric polarization with the applied electric field) of Gd substituted BSFO samples. All the materials have different breakdown voltage so the electric field was varied according to requirement and the driving frequency was kept constant at 50 kHz. At this fixed frequency, P_r increases with increasing external field thus, resulting in a higher driving power which is responsible for the increased reversal of spin moment [Fanggao *et al.* 2006]. However, saturation has not been achieved within the limit of applied electric field, lossy and elliptical loops were obtained [Scott 2007, Maglione *et al.* 2008, Jin *et al.* 2020].

4.3 Summary

The Gd substituted $Bi_{0.9-x}Sm_{0.1}Gd_xFeO_3$ (x =0.0, 0.025, 0.05, 0.075 and 0.1) samples are synthesized successfully using solid-state ceramic route. The increase in grain size up to x = 0.05 confirms the solubility limit up to x = 0.05. The structural and microstructural studies suggest the transformation of phase from rhombohedral to pseudocubic phase for $x \geq 0.075$. Also, the composition with x =0.075, i.e., $Bi_{0.825}$ $Sm_{0.1}Gd_{0.075}FeO_3$ possess all the ferroic properties *viz.*, high dielectric permittivity, low tangent loss and higher magnetization with significantly enhanced as compared to pure bismuth ferrite and samarium substituted bismuth ferrite. Most importantly, in the temperature range 80 to 300 °C, the $Bi_{0.825}$ $Sm_{0.1}Gd_{0.075}FeO_3$ sample follows Arrhenius behavior with almost single slope with significantly enhanced conductivity. Thus, we conclude that with the A-site double substitution on BFO not only enhance the ferroic feature but also increase the applicability of bismuth ferrite-based perovskites for ceramic applications by suppressing the dielectric anomalies of bismuth ferrite.